New kagome prototype materials: discovery of KV_3Sb_5, RbV_3Sb_5, and CsV_3Sb_5

Brenden R. Ortiz,[1,2,*] Lídia C. Gomes,[3,4] Jennifer R. Morey,[5] Michal Winiarski,[5,6] Mitchell Bordelon,[2] John S. Mangum,[1] Iain W. H. Oswald,[7] Jose A. Rodriguez-Rivera,[8,9] James R. Neilson,[7] Stephen D. Wilson,[2] Elif Ertekin,[3,4] Tyrel M. McQueen,[5] and Eric S. Toberer[1]

[1]*Colorado School of Mines, Golden, Colorado 80401, USA*
[2]*University of California Santa Barbara, Santa Barbara, California 93106, USA*
[3]*University of Illinois at Urbana-Champaign, Urbana, Illinois 61820, USA*
[4]*National Center for Supercomputing Applications, Urbana, Illinois 61801, USA*
[5]*Johns Hopkins University, Baltimore, Maryland 21218, USA*
[6]*Gdansk University of Technology, Gdansk 80-233, Poland*
[7]*Colorado State University, Fort Collins, Fort Collins, Colorado 80523, USA*
[8]*NIST Center for Neutron Research, Gaithersburg, Maryland 20878, USA*
[9]*University of Maryland, College Park, Maryland 20742, USA*

(Received 27 February 2019; revised manuscript received 21 June 2019; published 16 September 2019)

In this work, we present our discovery and characterization of a new kagome prototype structure, KV_3Sb_5. We also present the discovery of the isostructural compounds RbV_3Sb_5 and CsV_3Sb_5. All materials exhibit a structurally perfect two-dimensional kagome net of vanadium. Density-functional theory calculations indicate that the materials are metallic, with the Fermi level in close proximity to several Dirac points. Powder and single-crystal syntheses are presented, with postsynthetic treatments shown to deintercalate potassium from single crystals of KV_3Sb_5. Considering the proximity to Dirac points, deintercalation provides a convenient means to tune the Fermi level. Magnetization measurements indicate that KV_3Sb_5 exhibits behavior consistent with a the Curie-Weiss model at high temperatures, although the effective moment is low ($0.22\mu_B$ per vanadium ion). An anomaly is observed in both magnetization and heat capacity measurements at 80 K, below which the moment is largely quenched. Elastic neutron scattering measurements find no obvious evidence of long-range or short-range magnetic ordering below 80 K. The possibility of an orbital-ordering event is considered. Single-crystal resistivity measurements show the effect of deintercalation on the electron transport and allow estimation of the Kadowaki-Woods ratio in KV_3Sb_5. We find that $A/\gamma^2 \sim 61$ μOhm cm mol_{FU}^2 K^2 J^{-2}, suggesting that correlated electron transport may be possible. KV_3Sb_5 and its cogeners RbV_3Sb_5 and CsV_3Sb_5 represent a new family of kagome metals, and our results demonstrate that they deserve further study as potential model systems.

DOI: 10.1103/PhysRevMaterials.3.094407

I. INTRODUCTION

With its unique and elegant structure, few materials are as intensely studied in the field of condensed matter physics as the kagome lattice. A sister to the more common hexagonal tiling of graphene, the kagome lattice (trihexagonal tiling) stands out as a model system for the genesis of unconventional electronic and magnetic properties. The additional chemical complexity enables tuning of the underlying electronic and magnetic structures, enabling the kagome lattices to host a wide range of exotic physics. From topologically nontrivial band structures with Dirac points to quantum disordered magnetic ground states, the kagome lattices are keenly poised at the intersection of material science and physics.

The unconventional electronic states inherent to kagome lattices can be broadly categorized into the insulating and metallic (or semimetallic) categories. Specifically, the more widely explored insulating kagome lattices are most commonly studied in the frame of frustrated magnetism. One of the most noteworthy is $ZnCu_3(OH)Cl_2$, which has been proposed as a quantum spin liquid candidate [1–5]. The relatively less explored metallic and semimetallic variants are of increasing interest due to their potential to manifest nontrivial topologies and unique electronic structures endemic to a kagome lattice of metal ions. For example, recent studies of Fe_3Sn_2 have shown that ferromagnetism leads to the splitting of the spin-degenerate Dirac bands, creating a topologically nontrivial phase and a two-dimensional (2D) "Chern gap" [6]. Additionally, within the metal $Co_3Sn_2S_2$, a large anomalous Hall response and a favorable Berry curvature make it an attractive Weyl semimetal candidate [7]. Particularly within the metallic kagome lattices, the delocalization of electrons provides an additional degree of freedom. The formation of composite states through metallic bonding can cause a dramatic renormalization of the electronic and magnetic ground states. Prominent examples of similar behavior have been observed in the electronic instabilities of the cluster magnets GaV_4S_8 [8,9] and $LiZn_2Mo_3O_8$ [10–12].

This work presents our discovery of a new family of kagome metals: KV_3Sb_5, RbV_3Sb_5, and CsV_3Sb_5. In addition to powder synthesis, we present our method for growing single crystals of all three materials. All three materials

*Author to whom all correspondence should be addressed: ortiz.brendenr@gmail.com

possess a structurally perfect, 2D kagome lattice of vanadium. Density functional theory (DFT) calculations further confirm the dispersionless bands and Dirac points expected of a kagome system. Further, we find that many Dirac points are in close proximity to the Fermi level, making these systems attractive candidates for further study.

This work also presents experimental transport, magnetic, and structural data on KV_3Sb_5. Postsynthetic treatments of single crystals are successful in leeching potassium from KV_3Sb_5, providing a convenient means to manipulate the Fermi level (E_F). Magnetization measurements on powders and single crystals of KV_3Sb_5 exhibit behavior consistent with Curie-Weiss behavior at high temperatures, although the effective moment is quite low ($0.22\mu_B$ per vanadium). The low moment may be indicative of a small concentration of impurity spins. An anomaly is noted in both heat capacity and magnetization at 80 K, below which the moment appears largely quenched. Although elastic neutron scattering experiments fail to detect long-range or short-range magnetic ordering within our resolution ($\sim 0.5\mu_B$/atom), forms of orbital-ordering are still possible. Resistivity measurements on KV_3Sb_5 are indicative of a semimetal or "bad-metal," consistent with the calculated density of states. Further, we find that the Kadowaki-Woods ratio is quite large in KV_3Sb_5 (~ 61 μOhm cm mol_{FU}^2 K^2 J^{-2}), suggesting correlated transport is possible. Together, these results set the stage for future studies in a new class of kagome metals.

II. METHODS

A. Experiment

Powders and single crystals of KV_3Sb_5, RbV_3Sb_5, and CsV_3Sb_5 were synthesized from K (ingot, Alfa 99.8%), Rb (ingot, Alfa 99.75%), Cs (liquid, Alfa 99.98%), V (powder, Sigma 99.9%), and Sb (shot, Alfa 99.999%). Powders were synthesized by ball-milling elemental reagents for 1 h in a Spex 8000D high-energy ball mill. To avoid iron contamination, tungsten carbide vials and balls were used. Powders were subsequently ground, sieved through a 50 micron mesh, and annealed for 48 h at 600 °C. Single crystals are synthesized via the flux method. For KV_3Sb_5, low melting point eutectics between KSb_2-KSb or KSb_2-Sb make for convenient fluxes [13]. Flux mixtures containing 5 mol % of KV_3Sb_5 were heated to 1000 °C, soaked for 24 h, and subsequently cooled at 2 °C/h. Analogous reactions were performed for RbV_3Sb_5 and CsV_3Sb_5.

The prototype structure (KV_3Sb_5) was first solved using powder diffraction data collected at the Advanced Photon Source (11-BM) with 0.412 619 Å, radiation. Powders were sealed in Kapton capillaries after being diluted at a molar ratio of 1:4 with amorphous SiO_2 to reduce x-ray absorption. Structure solution was performed using charge-flipping methods and the TOPAS V6 software package [14–17]. Subsequent single-crystal diffraction was performed on a Bruker D8 Quest ECO diffractometer equipped with a microfocus Mo $K\alpha$ radiation source and a Photon 50 CMOS half-plate detector. Structure solutions were completed using SHELXT and the intrinsic phasing method [18,19]. Structures were verified through the PUBLCIF program [20]. Powder neutron diffraction data were collected on the MACS cold triple-axis spectrometer at the National Institute of Standards and Technology (NIST) Center for Neutron Research. Elastic measurements utilized Be filters to produce fixed initial and final energies of 5.0 meV.

Magnetization measurements were performed using a Quantum Design Magnetic Properties Measurement System (MPMS3). Densified powders and single crystals of KV_3Sb_5 were adhered to a Quantum Design quartz sample holder using GE varnish. Heat capacity and resistivity measurements (2–260 K) were performed using a Quantum Design Dynacool Physical Properties Measurement System (PPMS). Apiezon N-grease was used for thermal coupling of the sample to the heat capacity stage. Resistivity measurements were performed using a probe current of 0.999 mA. Additional heat capacity measurements from 0.055 to 3.5 K were performed with a Quantum Design Dilution Refrigerator.

Scanning electron microscopy (SEM) and energy-dispersive spectroscopy (EDS) were performed using a JEOL JSM-7000F FESEM. High-resolution transmission electron microscopy (HRTEM) micrographs were acquired on an FEI Talos F200X TEM operating at an accelerating voltage of 200 keV. For TEM, crystals of KV_3Sb_5 were crushed and sonicated in isopropyl alcohol to create a suspension. The suspension was dropped onto carbon TEM grids. Selective, structure-factor-based Fourier filtering of reflections was used to decouple the V1-K1 and Sb1-Sb2 sublattices from each other. Further deconvolution of the V1 and K1 sublattices was performed on the basis of ionic radii.

B. Computational

The electronic structure of KV_3Sb_5, RbV_3Sb_5, and CsV_3Sb_5 was calculated using Kohn-Sham density functional theory (DFT) as implemented in the VASP software package [21–23]. Core and valence electrons were treated within the projected augmented wave (PAW) formalism [24]. The generalized-gradient approximation (GGA) is used for the exchange-correlation term within the Perdew-Burke-Ernzerhof (PBE) approach [25]. The Kohn-Sham orbitals were expanded using a plane-wave basis with a cutoff energy of 500 eV. Structural optimization of the lattice parameters and atomic positions was performed with a stringent force tolerance of 1 meV/Å on each atom. The Brillouin zone was sampled using a Γ-centered $8 \times 8 \times 4$ Monkhorst-Pack k-point grid [26]. Crystal orbital Hamilton population (COHP) analysis was performed using the LOBSTER package in conjunction with VASP [22,23,27]. Note that the COHP analysis was performed using a finer k-point mesh of $12 \times 12 \times 6$. Total energies of the magnetic systems were calculated with the DFT + U approach, as proposed by Dudarev *et al.* [28]. The additional Hubbard-like term is used to treat the on-site Coulomb interactions on the localized d-states of vanadium atoms. In this case, $2 \times 2 \times 1$ supercells are used to model the different spin configurations.

III. RESULTS AND DISCUSSION

We begin with a structural analysis of KV_3Sb_5, RbV_3Sb_5, and CsV_3Sb_5 through powder and single-crystal x-ray diffraction, providing a conceptual interpretation of the new

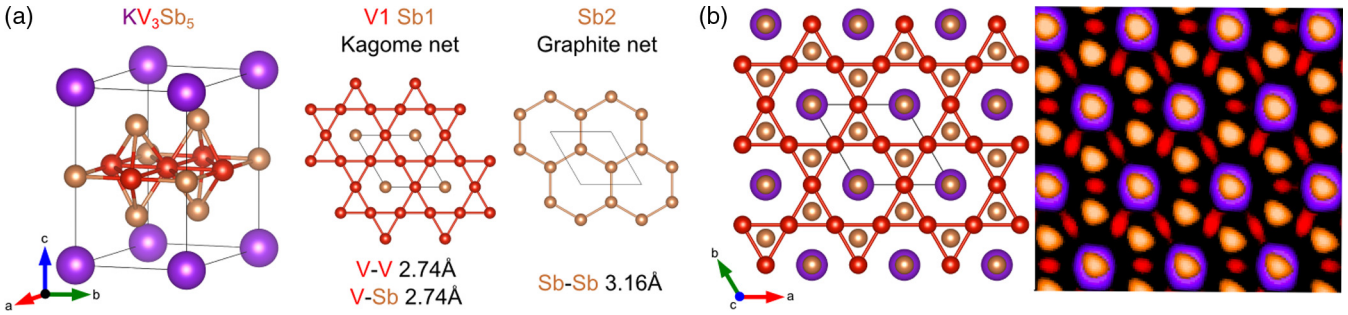

FIG. 1. The prototype structure KV_3Sb_5 (a) crystallizes in the $P6/mmm$ space group and exhibits a layered structure of V-Sb sheets intercalated by K. The vanadium sublattice is a structurally perfect kagome lattice. There are two distinct Sb sublattices. The sublattice formed by the Sb1 atom is a simple hexagonal net, centered on each kagome hexagon. The Sb2 sublattice creates a graphenelike Sb sheet below and above each kagome layer. Bond distances for the V-V, V-Sb, and Sb-Sb nearest-neighbor interactions are also shown. Fourier-filtered, false-colored atomic resolution TEM (b) is able to partially decouple the Sb sublattices (orange) from the K-V (red and purple) sublattices. While we cannot mathematically separate the K and V sublattices during Fourier analysis, the large ionic radius of K is evident from visual inspection alone.

structural prototype. We also provide evidence for the deintercalation of potassium in KV_3Sb_5. Afterward, we provide an extensive overview of the electronic structure in all three materials, examining the electron band diagrams, density of states, and crystal orbital Hamilton population. We have focused our experimental characterization efforts on KV_3Sb_5, examining magnetization, neutron scattering, and heat capacity experiments on polycrystalline powders. The effect of deintercalation on single-crystal resistivity measurements is also investigated.

A. Discovery and crystal structure

The discovery of KV_3Sb_5, RbV_3Sb_5, and CsV_3Sb_5 emerged from our search for new transition-metal Zintl antimonides for thermoelectric applications [29,30]. The prototype KV_3Sb_5 was first isolated in powders, and the structure was solved using charge-flipping methods on powder diffraction data. The resulting Rietveld refinement and associated crystallographic information are shown in Fig. S1 of the Supplemental Material [31]. Once we had identified KV_3Sb_5 as a new prototype structure, we explored all combinations of (K,Rb,Cs)(V,Nb,Ta)(Sb,Bi) under a variety of synthesis conditions. Only KV_3Sb_5, RbV_3Sb_5, and CsV_3Sb_5 crystallize in the KV_3Sb_5 prototype. We did not attempt synthesis of the arsenide analogs due to toxicity concerns.

To validate the structures and to provide a more robust platform for future studies, we developed single-crystal syntheses for all three materials—details are outlined in Sec. II. Crystals recovered from flux growths are thin (10–100 microns), silver-colored platelets. The crystals range from 1 mm × 1 mm to 5 mm × 5 mm in area. The platelets will often exhibit natural hexagonal faceting. All materials are easily deformed, and the platelets show a natural tendency to exfoliate (Fig. S2) [31].

A summary of crystallographic parameters and refinement statistics obtained from single-crystal x-ray diffraction (SCXRD) for all three materials are provided in Tables S1–S4 of the Supplemental Material [31]. For KV_3Sb_5, we have included two refinements, one for the crystals grown in a KSb_2-KSb flux (etched in HNO_3) and another for crystals grown in a KSb_2-Sb flux (etched in water). A selection of precession images collected from the SCXRD for KV_3Sb_5 is also shown in Fig. S3 [31]. Consistent with the powder diffraction data, we find that KV_3Sb_5, RbV_3Sb_5, and CsV_3Sb_5 crystallize in the hexagonal $P6/mmm$ space group. All compounds consist of V-Sb slabs intercalated by alkali-metal cations [Fig. 1(a)]. Most notably, the vanadium sublattice forms a structurally perfect 2D kagome net. KV_3Sb_5 is a new kagome prototype structure, and is one of the smallest and simplest examples of a kagome lattice.

Due to the high symmetry of the $P6/mmm$ space group and the small unit cell, the KV_3Sb_5 prototype only possesses three structural degrees of freedom (a and c lattice parameters, z-coordinate on Sb2). An intuitive description of the KV_3Sb_5 prototype structure can be obtained by decomposing the structure into the individual atomic sublattices created by the atomic basis: K1, V1, Sb1, and Sb2. Figure 1(a) shows the V1 + Sb1 and Sb2 sublattices alongside the overall structure of KV_3Sb_5. As mentioned before, the vanadium sublattice is a structurally perfect kagome net. The kagome net of vanadium is interwoven with a simple hexagonal net formed by the Sb1 sites. From a space-filling perspective, the Sb1 atoms fill the natural gap formed in the kagome plane, which is reminiscent of Herbertsmithite [$ZnCu_3(OH)_6Cl_2$], where Zn ions occupy the centers of the kagome hexagons. The Sb2 layers at $c \sim 0.25$ and 0.75 form graphenelike networks of Sb that sandwich the kagome layer. Each V-Sb slab is separated by a simple hexagonal net of K formed by the K1 site.

In addition to the PXRD and SCXRD results, we also performed atomic resolution transmission electron microscopy (TEM) for platelets of KV_3Sb_5. Figure 1(b) shows the expected structure for KV_3Sb_5 along the [001] direction alongside a Fourier-filtered, false-colored TEM micrograph. Using Fourier-filtering, we were able to partially decouple the Sb sublattices (orange) from the V and K sublattices (red). While we were not able to mathematically decouple the V and K sublattices during Fourier analysis, the large ionic radii of K (purple) is quite apparent from visual inspection alone.

Despite the intercalated structure, powders, single crystals, and densified pellets of KV_3Sb_5, RbV_3Sb_5, and CsV_3Sb_5 are remarkably stable. Samples are stable in air for >1 year without decomposing or tarnishing. KV_3Sb_5 is stable under

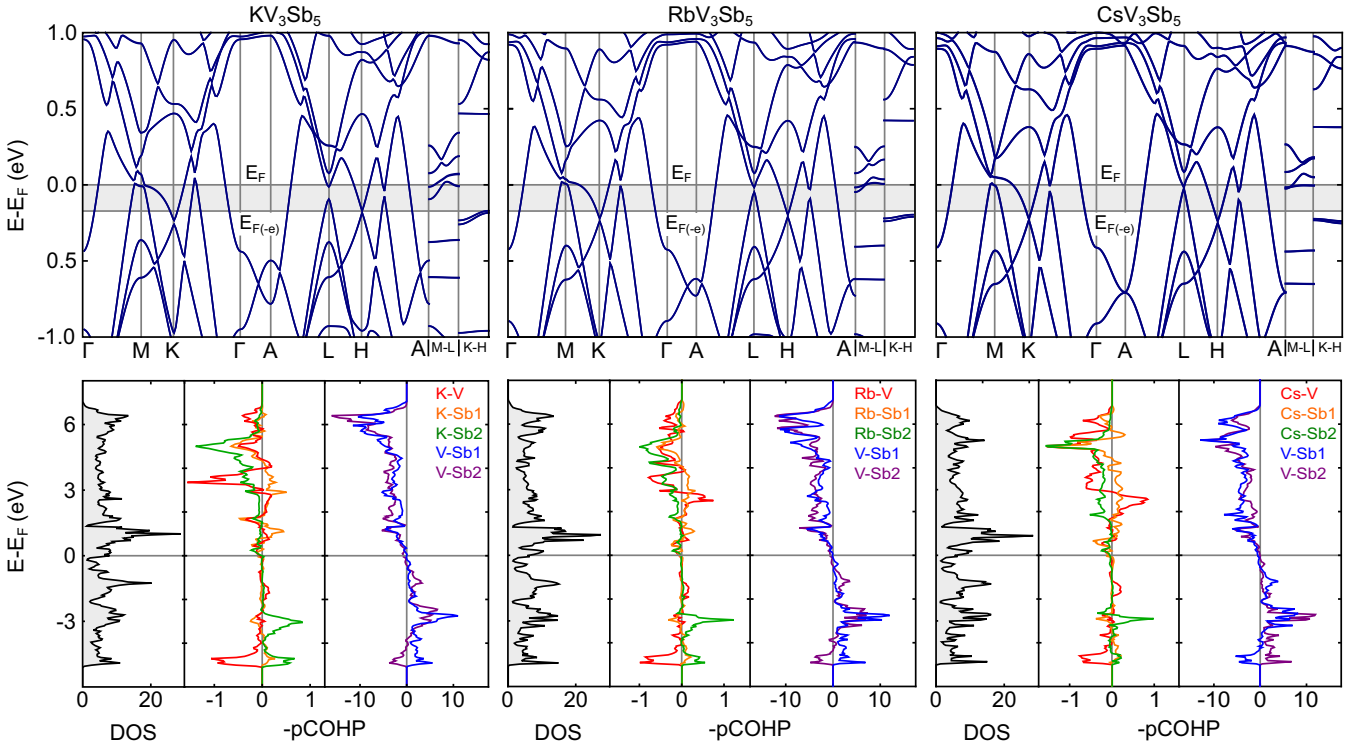

FIG. 2. First-principles calculations on KV_3Sb_5, RbV_3Sb_5, and CsV_3Sb_5 reveal that all three materials are metallic. Consistent with the kagome and graphenelike sublattices, the electronic structure exhibits multiple Dirac points near the Fermi level (E_F). Tuning of E_F is possible through experimental deintercalation of potassium. The range of E_F obtainable up to full deintercalation is indicated by $E_{F(-e)}$. The density of states (DOS) exhibits a local minima near E_F, suggesting that electron transport may show properties more indicative of a semimetal. Crystal orbital Hamilton population (COHP) investigates the relative contributions to bonding (positive) and antibonding (negative) interactions. For example, we find that the filled V-Sb1 interactions are entirely bonding up to E_F, demonstrating their role in structural stabilization. Conversely, all interactions involving K are weak, supporting our experimental deintercalation results.

cycling to cryogenic temperatures (<2 K). Densified pellets also tolerate temperatures up to 600 °C under vacuum, with no observable sublimation. Single-crystal samples are not affected by common solvents (e.g., isopropyl, ethanol, acetone) and water, with no apparent reaction while submerged. Within the resolution of XRD and EDS, all samples prepared using solid-state methods exhibit fully occupied K1 sites, regardless of whether the powder synthesis is performed under K-rich or K-poor conditions. Reminiscent of the process of "phase boundary mapping" from thermoelectrics [32–35], this suggests that the single-phase width of KV_3Sb_5 accessible from solid-state synthesis reactions is small. However, when crystals are etched in concentrated HNO_3, SCXRD suggests that the K1 occupancy is depleted to approximately 85%. When the crystals are only treated with purified water, SCXRD measurements show that the K1 occupancy remains at 92%. While the changes in potassium occupancy are subtle, we note that the refined values track changes in the cell volume quite well: powder (100% occupied, 233.15 $Å^3$), water-etched crystals (92% occupied, 232.86 $Å^3$), acid-etched crystals (85% occupied, 231.93 $Å^3$).

B. Electronic structure

As KV_3Sb_5, RbV_3Sb_5, and CsV_3Sb_5 are entirely new materials, our investigation first focuses on an in-depth study of the electronic structure and bonding through first-principles density functional theory (DFT) calculations. The band diagrams of KV_3Sb_5, RbV_3Sb_5, and CsV_3Sb_5 (Fig. 2, top) are presented along the electronic density of states (DOS) and associated crystal orbital Hamilton population (COHP) analysis (Fig. 2, bottom). All calculations were performed using spin-orbit coupling. Except for a few avoided crossings in the relativistic result, we do not observe significant changes from the inclusion of spin-orbit coupling. Although we did not study the arsenides experimentally, first-principles calculations of the band diagrams are available in Fig. S4 [31]. In general, the band structures are very similar between KV_3Sb_5, RbV_3Sb_5, and CsV_3Sb_5. One difference of note, however, is the gap at L, which narrows significantly as we transition from KV_3Sb_5 to CsV_3Sb_5.

All of the structures presented here are metallic, although there are a relatively limited number of band crossings near the Fermi level (E_F). Besides a set of dispersive bands near Γ and A, the majority of band crossings occurs due to Dirac-like features at H, K, L, and even H-A. An interesting feature of the band diagram emerges if one examines the features at K and H. These are not isolated Dirac cones; if we consider the dispersion along K-H, we see that the features are connected, forming a conical valley. We note that E_F in these materials is remarkably close to several of the Dirac crossings (e.g., the H-point in KV_3Sb_5 is approximately 0.25 eV below E_F).

Coupled with the facile deintercalation of the alkali metal, the large number of Dirac points provides a key opportunity for these materials. For example, the deintercalation of potassium in KV_3Sb_5 is a particularly attractive way to tune E_F, as we would not need to introduce any extrinsic dopants. A similar phenomenon has been observed in KNi_2Se_2, where potassium was removed through oxidative deintercalation [36]. The removal of one electron per unit cell, corresponding to complete deintercalation of K, is shown on the electronic structures in Fig. 2 (shaded). Bader charge analysis indicates that the K atoms each transfer one electron to the V-Sb layer, leaving behind empty K 4*s* states that appear in the unfilled levels above the Fermi energy. We further observe limited to no charge sharing between the K and the V-Sb layer, suggesting that the bonding *between* the K and V-Sb layers may be primarily driven by electrostatics. This is supported by electronic structure calculations on the hypothetical compound V_3Sb_5 (Fig. S5), where the electronic structure near E_F is largely unperturbed by the removal of potassium [31]. To understand why these systems tolerate alkali-metal deintercalation, we turn to the bonding and chemical information provided by COHP.

COHP (Fig. 2, bottom) partitions the band diagram into orbital-pair interactions, allowing us to resolve bonding and antibonding contributions from individual atomic orbitals. Integrating the contribution from each atom allows us to gain a sense of bond strength, allowing for a chemically intuitive interpretation of the electronic structure. All COHP results are shown alongside the electronic DOS in Fig. 2. All symmetry-unique nearest-neighbor interactions have been included. The middle panel (red, orange, green) shows the COHP for bonds involving K atoms while the rightmost panel (blue, purple) shows the COHP for bonds between V and Sb atoms. Consistent with the large bond distance between K and the V-Sb layers, the magnitude of the COHP is much smaller for pairwise interactions with K (note the order-of-magnitude difference in the *x*-axis scale). We can see that the majority of the bonding interactions occurs between V and Sb, as expected. In particular, the filled V-Sb1 bonds are entirely bonding in nature, suggesting that the Sb1 atoms woven into the kagome lattice play a large role in the structure's stability. Both Bader and COHP analysis suggests that the K atoms are very loosely bound to the structure—supporting deintercalation as a means to tune E_F.

C. Magnetization and heat capacity of KV_3Sb_5

As a new prototype kagome lattice, a natural question is whether there is any experimental evidence of magnetism in these systems. Both powders and single-crystal samples of KV_3Sb_5 were measured under a series of temperatures and fields. In the main body, we present magnetization data and heat capacity data on sintered polycrystalline samples of phase-pure KV_3Sb_5. Despite single crystals having appreciable dimensions (>1 mm × 1 mm), the samples are very thin (10–100 micron) and are not accurately massed. As such, multiple crystals (∼20–50) must be coaligned. While alignment along the *c*-axis is relatively easy, not all crystals exhibit faceting, diminishing our ability to extract orientation-specific information. Further, the small sample masses and low moment make polycrystalline samples more quantitatively accurate for this study. However, the qualitative behavior of the single crystals is still valuable as a comparison, and is included in Fig. S6 [31].

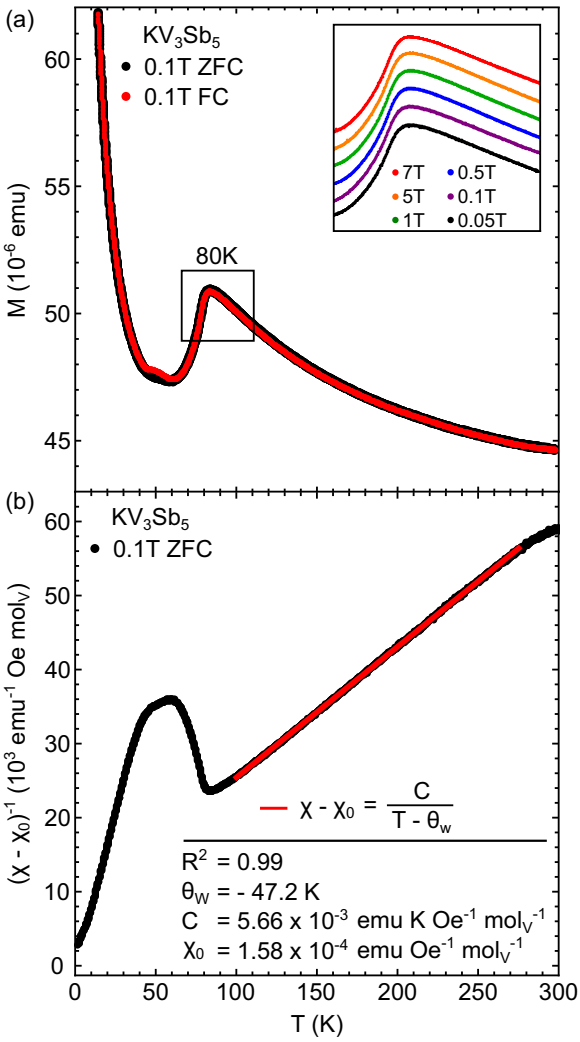

FIG. 3. Magnetization measurements (a) on polycrystalline KV_3Sb_5 exhibit localized moment behavior at high temperatures. An anomaly is noted at 80 K, below which the localized moment is quenched. The transition persists in both field-cooled (FC) and zero-field-cooled (ZFC) data. Further, the anomaly is unaffected by application of fields up to 7 T (inset). The inverse susceptibility data (b) is well characterized by a Curie-Weiss model (red). The χ_0 correction was empirically determined, although estimates of the Pauli paramagnetic response in KV_3Sb_5 are consistent with the result. Curie-Weiss analysis reveals a small effective moment $\mu_{\text{eff}} \sim 0.22\mu_B$ per vanadium.

Figure 3(a) shows temperature-dependent magnetization measurements performed on polycrystalline KV_3Sb_5 under a 0.1 T field. Both the zero-field-cooled (ZFC, black) and field-cooled (FC, red) data are shown. A significant anomaly is noted at 80 K in both the ZFC and FC data. The transition is unaffected, both in temperature and magnitude, by application of magnetic fields up to 7 T (see Fig. 3, inset). Another small anomaly appears below the transition (40–65 K), however it

is only apparent in the FC data. This feature is also retained under the application of various fields. We note that the primary anomaly at 80 K is also observed in single-crystal measurements (Fig. S6) [31].

For the data above the primary anomaly at 80 K, KV_3Sb_5 exhibits behavior consistent with the Curie-Weiss model. As such, Fig. 3(b) investigates a Curie-Weiss model on the inverse susceptibility. Using an empirically determined χ_0 correction of 1.58×10^{-4} emu Oe^{-1} mol_V^{-1}, the high-temperature data are well fit by the Curie-Weiss model with a Weiss temperature of -47.2 K and a Curie constant of 5.66×10^{-3} emu K Oe^{-1} mol_V^{-1}. We estimate $\mu_{\text{eff}} \sim 0.22\mu_B$ per vanadium. We note that the high-temperature data can also be approximated using a Curie model ($\theta_W = 0$). While the effective moment is relatively unchanged between the Curie and Curie-Weiss models, the fit is visibly better for the Curie-Weiss approach.

As a check on the magnitude of χ_0, we can estimate the expected Pauli paramagnetic response of KV_3Sb_5. Using the typical expression $\chi_P = \mu_0\mu_B^2 g(E_F)$, where $g(E_F)$ is the density of states at the Fermi level determined by DFT (see Fig. 2), we obtain $\chi_P \sim 0.84 \times 10^{-4}$ emu Oe^{-1} mol_V^{-1}, in excellent agreement with the empirically determined value (1.58×10^{-4} emu Oe^{-1} mol_V^{-1}). Some divergence from the Curie-Weiss fit is noted near room temperature. At these temperatures, however, the background magnetization expected from the χ_0 term is comparable to the measured values. As such, some divergence is to be expected.

Although simple charge-counting arguments suggest that the expected moment in KV_3Sb_5 should be small, our magnetization results found a mere $0.22\mu_B$ per vanadium. Consider the localized limit; assuming potassium exists as K^+ and antimony as Sb^{3-}, we require 14 electrons from the 3 vanadium atoms. This could be achieved by having 2 vanadium atoms in the V^{5+} state (d^0, diamagnetic) and 1 in the V^{4+} state (d^1, magnetically active). On average, this schema would leave one spin per KV_3Sb_5 formula unit, which is still significantly larger (even at the $J = 1/2$ limit) than our observed values. As a check, we estimated the impurity spin concentration that could yield similar results. We estimate that our effective magnetization observed at high temperatures could be explained with an effective concentration of 1.5% ($S = 1/2$) impurity spins on the vanadium sites, which is a reasonable result considering the propensity for potassium vacancy formation.

Noting that the low-temperature data in Fig. 3 also show data consistent with a Curie tail (impurity spins), we also examined magnetization versus field measurements (Fig. S7) at 2, 60, 100, 200, and 325 K from 0 to 7 T [31]. All temperatures except for the 2 K measurement exhibit linear magnetization curves with no hysteresis or remnant magnetization, confirming that there are no bulk ferromagnetic contributions to the magnetism in KV_3Sb_5. The magnetization versus field data at 2 K shows signs of a saturation magnetization, which was modeled with a Brillouin function (Fig. S8) to estimate the concentration of unpaired impurity spins [31]. Assuming that these impurities would behave as $J = 1/2$ spins with a Landé g-factor of 2, we find that the magnetization response could be explained by an impurity concentration of 0.12% on the vanadium sites. Considering our approximations, the Curie-Weiss and low-temperature Brillouin fits are both consistent with a small fraction of impurity spins.

Considering the kagome structure and the magnetization anomaly, the potential for antiferromagnetic order was explored via elastic neutron diffraction. Measurements were taken above (110 K) and below (1.8 K) the 80 K anomaly (Fig. S9) [31]. There are no signs of diffuse scattering (short-range correlations) or new magnetic peaks brought about by magnetic ordering within the experimental resolution ($\sim 0.5\mu_B$/atom). Even in the localized limit (charge counting), KV_3Sb_5 would be expected to exhibit a low moment—challenging even for high-flux neutron experiments. Our experiments also do not rule out more subtle forms of ordering such as orbital-ordering. For example, a trimerization event akin to the effect observed in $NaVO_2$ [37] would not be detectable by our current experiment. The possibility of trimerization is particularly interesting, as this would transform the kagome crystal lattice into a honeycomb spin lattice. Regardless, additional studies are underway to unravel the underlying magnetic structure of KV_3Sb_5.

Heat-capacity measurements (Fig. 4) on a sintered fragment of KV_3Sb_5 reveal trends consistent with magnetization data. A small anomaly is noted at 80 K. The anomaly is unaffected by field, and no appreciable shift is noted between the zero-field (black) and 7 T (red) measurements. Despite the prominent transition in the magnetization results, the heat capacity anomaly is comparatively weaker. The transition is also somewhat unusual in shape, and is not consistent with a λ-type transition or a Schottky anomaly. This is consistent with the lack of an obvious magnetic ordering event in the elastic neutron data. A sharp upturn in the heat capacity is noted at dilution fridge temperatures (~0.25 K), which is

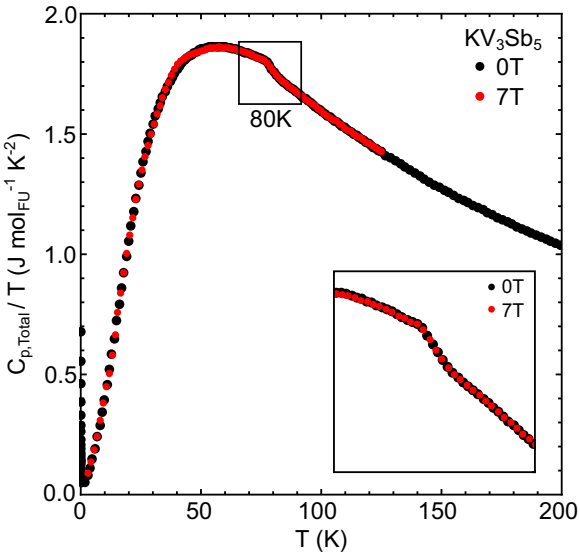

FIG. 4. Heat-capacity measurements (C_p/T) on KV_3Sb_5 also present with an anomaly at 80 K, consistent with magnetization results. Heat-capacity results are unaffected by application of a 7 T field (red). While quite prominent in the magnetization results, the primary anomaly at 80 K is only weakly present in the heat-capacity data (inset), and it does not appear indicative of a λ-type transition or Schottky anomaly.

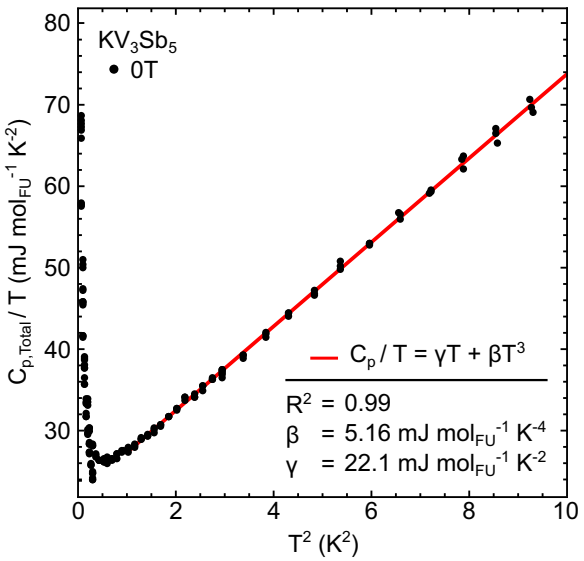

FIG. 5. Low-temperature dilution refrigerator (0.07–3 K) zero-field heat-capacity (C_p/T) measurements on KV_3Sb_5 are well modeled with a sum of electron and phonon contributions (Sommerfeld model, red curve). We note that the Sommerfeld coefficient γ is relatively large when compared to elemental metals. The strong increase in the heat capacity at low temperature (∼0.25 K) is most likely related to onset of a nuclear contribution.

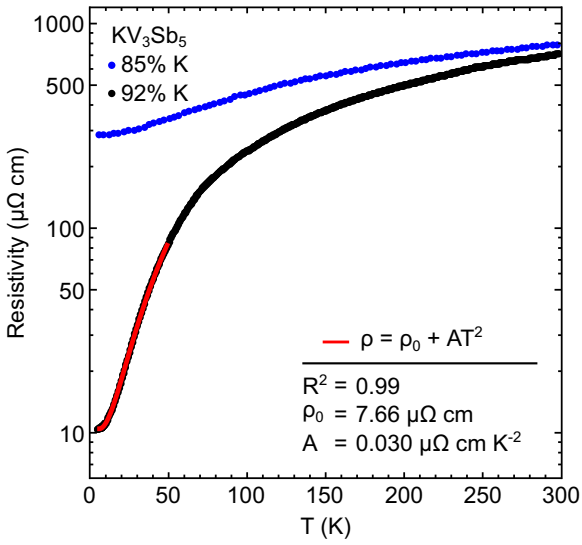

FIG. 6. In-plane electrical resistivity measurements on KV_3Sb_5 single crystals reveal metallic transport, although the resistivity at room temperature (∼0.5 mOhm cm) is more typical of a heavily doped semimetal or "bad-metal." As a metric for correlated electron transport (e.g., heavy fermions), a quadratic fit (red) to the low-temperature resistivity was used to extract the temperature-dependent parameter A. In conjunction with heat-capacity data, A can be used to calculate the Kadowaki-Woods ratio.

likely a nuclear contribution. Figure 5 shows a magnified version of the low-temperature heat capacity. Note that the bottom axis in Fig. 5 is scaled as T^2. The data are well-modeled with the Sommerfeld model ($C_p = \gamma T + \beta T^3$). The Sommerfeld coefficient γ evaluates to 22.1 mJ $\text{mol}_{\text{FU}}^{-1}\,\text{K}^{-2}$, which is relatively large when compared to simple elemental metals.

With the ambiguity between the localized moment model and the impurity spins, our first-principles calculations were reexamined to check for changes in the total energy with the addition of localized spin. As standard DFT methods (GGA-PBE) rarely treat d- and f-orbitals accurately, we employed the DFT + U method to treat electron-electron interactions within the vanadium d-orbitals [28]. Unfortunately, U is difficult to determine *a priori*. Therefore, we performed calculations with $U = 0$, $+1$, $+3$, and $+5$, which are typical values for vanadium [38–40]. We considered ferromagnetic, ferrimagnetic, and antiferromagnetic configurations in supercells of KV_3Sb_5. As the structure is frustrated, five distinct (disordered) antiferromagnetic configurations were evaluated. The different configurations and associated energies are shown in Figs. S10 and S11 and Table S5 [31]. The total energy in DFT appears to decrease linearly with the number of antiferromagnetic nearest-neighbor configurations, as in a simple nearest-neighbor Heisenberg exchange interaction. Thus, in DFT, the spin lattice shows a robust tendency to antialign locally, regardless of long-range symmetry.

D. Electron transport and Fermi level tuning in KV_3Sb_5

The small mass of the KV_3Sb_5 single crystals made powders the most robust platform for our initial studies into the magnetic and thermodynamic properties. However, the single crystals are the ideal form factor for resistivity. Additionally, resistivity measurements should be quite sensitive to the deintercalation of potassium—allowing us to examine the effect of our postsynthetic treatments on single crystals.

To test the effect of K deintercalation on the transport properties of KV_3Sb_5, we performed resistivity measurements on single crystals grown through the flux method. Figure 6 shows measurements on crystals with two different levels of potassium deintercalation. The blue curve corresponds to crystals that were etched in hot HNO_3 and show a significant reduction in potassium content ($K_{0.85}V_3Sb_5$). The black curve corresponds to crystals that are treated with water only, and show near stoichiometric compositions ($K_{0.92}V_3Sb_5$). As we deintercalate potassium, we observe an increase in the electronic resistivity, particularly at low temperatures. This is consistent with a decrease in the number of charge carriers, however we must also be cautious of possible damage caused by aggressive etching. Consistent with DFT, KV_3Sb_5 exhibits metallic transport, although the resistivity (∼0.5 mOhm cm at 300 K) is significantly higher than that expected of an elemental metal, suggesting that these materials more closely resemble semimetals or "bad metals."

At low temperatures (where electron-electron scattering dominates electron-phonon scattering), the electronic resistivity can be modeled by $\rho = \rho_0 + AT^2$. For the higher occupancy crystals (black), we estimate the quadratic component of the resistivity to be approximately 0.030 μOhm cm K^{-2}. The resulting fit is shown in Fig. 6 (red curve). A zoomed-in version of the quadratic fit can be found in Fig. S12 [31]. The quadratic resistivity term can be subsequently combined with the linear (electronic) term from the low-temperature heat

capacity data to estimate the Kadowaki-Woods ratio (KWR) in KV_3Sb_5. The Kadowaki-Woods ratio (A/γ^2) is commonly used as a metric to probe the potential for correlated electron transport [41]. We estimate the KWR in crystals of $K_{0.92}V_3Sb_5$ to be approximately 61 μOhm cm mol_{FU}^2 K^2 J^{-2}. At this time, our results do not take into account dimensionality or electron density corrections to the KWR [42]. However, the result is typical of materials that exhibit heavy fermion behavior ($\sim$10 μOhm cm mol^2 K^2 J^{-2}), which suggests that KV_3Sb_5 may be a candidate material for correlated electron transport.

IV. CONCLUSION

Despite the relatively narrow suite of kagome lattices, almost all of them exhibit unique and interesting phenomena. This work introduced a new, structurally intuitive kagome prototype (KV_3Sb_5) and three new materials (KV_3Sb_5, RbV_3Sb_5, CsV_3Sb_5). All three compounds exhibit structurally perfect kagome networks of vanadium. Furthermore, KV_3Sb_5 is currently one of the smallest and simplest kagome lattices available within the literature. We have developed powder and single-crystal syntheses for all three materials, proving robust samples for investigation of the electronic, magnetic, and thermodynamic properties. Using density functional theory (DFT), we have performed a detailed analysis of the electronic structure and bonding within KV_3Sb_5, RbV_3Sb_5, and CsV_3Sb_5. As expected of the kagome and graphitelike sublattices, the Fermi level is in close proximity to several Dirac points. Considering the facile deintercalation of the alkali metal, postsynthetic methods may provide a convenient means to tune E_F to the Dirac points. Magnetization measurements indicate behavior consistent with a localized moment at high temperatures, although the signal could originate from a small fraction of $S = 1/2$ impurity spins. An anomaly is observed in both magnetization and heat-capacity measurements at 80 K, below which the local moment is largely quenched. Neutron scattering was unable to resolve signatures of long-range or short-range magnetic ordering below the magnetization anomaly. Orbital ordering events (e.g., trimerization) are still possible, although more evidence is required to confirm. Resistivity and heat capacity measurements reveal a large KWR, suggesting the possibility of correlated transport. The combination of a new kagome prototype structure, three new materials, Fermi level tuning through deintercalation, and the potential for correlated transport sets a solid foundation for further experimental and computational studies within these new compounds.

ACKNOWLEDGMENTS

B.R.O. and E.S.T. acknowledge support from the National Science Foundation, Grant No. 1729594. B.R.O. also acknowledges support from the California NanoSystems Institute through the Elings Fellowship program. L.C.G. and E.E. acknowledge support from the National Science Foundation, Grants No. 1729149 and No. 1437106. J.R.M. and M.W. acknowledge support from the Institute for Quantum Matter, U.S. Department of Energy, Office of Science, Office of Basic Energy Sciences, under Award No. DE-SC0019331. T.M.M. acknowledges the David and Lucile Packard Foundation, and the Johns Hopkins University Catalyst Award. J.R.N. and I.W.H.O. acknowledge support from the A.P. Sloan Foundation. E.S.T., J.R.N., and I.W.H.O. acknowledge the Research Corporation for Science Advancement through Cottrell Scholar Awards. S.D.W. and M.B acknowledge support from 538 DOE, Office of Science, Basic Energy Sciences under Award No. DE-SC0017752. M.B. also acknowledges support from the National Science Foundation Graduate Research Fellowship Program, Grant No. 1650114. M.W. was supported by the Foundation for Polish Science (FNP). The research reported here made use of shared facilities of the UCSB MRSEC (NSF DMR 1720256). Use of the Advanced Photon Source at Argonne National Laboratory was supported by the U.S. Department of Energy, Office of Science, Office of Basic Energy Sciences, under Contract No. DE-AC02-06CH11357. Access to MACS was provided by the Center for High Resolution Neutron Scattering, a partnership between the National Institute of Standards and Technology and the National Science Foundation under Agreement No. DMR-1508249. We thank Paul Sarte for the helpful discussion.

[1] D. E. Freedman, T. H. Han, A. Prodi, P. Müller, Q.-Z. Huang, Y.-S. Chen, S. M. Webb, Y. S. Lee, T. M. McQueen, and D. G. Nocera, Site specific x-ray anomalous dispersion of the geometrically frustrated kagomé magnet, herbertsmithite, $ZnCu_3(OH)_6Cl_2$, J. Am. Chem. Soc. **132**, 16185 (2010).

[2] D. Wulferding, P. Lemmens, P. Scheib, J. Roder, P. Mendels, S. Chu, T. Han, and Y. S. Lee, Interplay of thermal and quantum spin fluctuations in the kagome lattice compound herbertsmithite, Phys. Rev. B **82**, 144412 (2010).

[3] T. Han, S. Chu, and Y. S. Lee, Refining the Spin Hamiltonian in the Spin-1/2 Kagome Lattice Antiferromagnet $ZnCu_3(OH)_6Cl_2$ Using Single Crystals, Phys. Rev. Lett. **108**, 157202 (2012).

[4] T.-H. Han, J. S. Helton, S. Chu, D. G. Nocera, J. A. Rodriguez-Rivera, C. Broholm, and Y. S. Lee, Fractionalized excitations in the spin-liquid state of a kagome-lattice antiferromagnet, Nature (London) **492**, 406 (2012).

[5] M. Fu, T. Imai, T.-H. Han, and Y. S. Lee, Evidence for a gapped spin-liquid ground state in a kagome Heisenberg antiferromagnet, Science **350**, 655 (2015).

[6] L. Ye *et al.*, Massive Dirac fermions in a ferromagnetic kagome metal, Nature (London) **555**, 638 (2018).

[7] E. Liu *et al.*, Giant anomalous Hall effect in a ferromagnetic kagome-lattice semimetal, Nat. Phys. **14**, 1125 (2018).

[8] R. Pocha, D. Johrendt, and R. Pöttgen, Electronic and structural instabilities in GaV_4S_8 and $GaMo_4S_8$, Chem. Mater. **12**, 2882 (2000).

[9] H. Müller, W. Kockelmann, and D. Johrendt, The magnetic structure and electronic ground states of Mott insulators GeV_4S_8 and GaV_4S_8, Chem. Mater. **18**, 2174 (2006).

[10] J. P. Sheckelton, J. R. Neilson, D. G. Soltan, and T. M. McQueen, Possible valence-bond condensation in the frustrated cluster magnet $LiZn_2Mo_3O_8$, Nat. Mater. **11**, 493 (2012).

[11] M. Mourigal, W. T. Fuhrman, J. P. Sheckelton, A. Wartelle, J. A. Rodriguez-Rivera, D. L. Abernathy, T. M. McQueen, and C. L. Broholm, Molecular Quantum Magnetism in $LiZn_2Mo_3O_8$, Phys. Rev. Lett. **112**, 027202 (2014).

[12] J. P. Sheckelton *et al.*, Local magnetism and spin correlations in the geometrically frustrated cluster magnet $LiZn_2Mo_3O_8$, Phys. Rev. B **89**, 064407 (2014).

[13] J. Sangster and A. D. Pelton, The K-Sb (potassium-antimony) system, J. Phase Equilib. **14**, 510 (1993).

[14] G. Oszlányi and A. Sütö, *Ab initio* structure solution by charge flipping, Acta Crystallogr. A **60**, 134 (2004).

[15] G. Oszlányi and A. Sütö, *Ab initio* structure solution by charge flipping. II. use of weak reflections, Acta Crystallogr. A **61**, 147 (2005).

[16] G. Oszlányi, A. Sütő, M. Czugler, and L. Párkányi, Charge flipping at work: A case of pseudosymmetry, J. Am. Chem. Soc. **128**, 8392 (2006).

[17] A. Coelho, A charge-flipping algorithm incorporating the tangent formula for solving difficult structures, Acta Crystallogr. A **63**, 400 (2007).

[18] G. M. Sheldrick, SHELXT–Integrated space-group and crystal-structure determination, Acta Crystallogr. A **71**, 3 (2015).

[19] G. M. Sheldrick, Crystal structure refinement with SHELXL, Acta Crystallogr. C **71**, 3 (2015).

[20] S. P. Westrip, publCIF: software for editing, validating and formatting crystallographic information files, J. Appl. Crystallogr. **43**, 920 (2010).

[21] W. Kohn and L. J. Sham, Self-consistent equations including exchange and correlation effects, Phys. Rev. **140**, A1133 (1965).

[22] G. Kresse and J. Furthmüller, Efficiency of *ab-initio* total energy calculations for metals and semiconductors using a plane-wave basis set, Comput. Mater. Sci. **6**, 15 (1996).

[23] G. Kresse and J. Furthmüller, Efficient iterative schemes for *ab initio* total-energy calculations using a plane-wave basis set, Phys. Rev. B **54**, 11169 (1996).

[24] P. E. Blöchl, Projector augmented-wave method, Phys. Rev. B **50**, 17953 (1994).

[25] J. P. Perdew, K. Burke, and M. Ernzerhof, Generalized Gradient Approximation Made Simple, Phys. Rev. Lett. **77**, 3865 (1996).

[26] H. J. Monkhorst and J. D. Pack, Special points for Brillouin-zone integrations, Phys. Rev. B **13**, 5188 (1976).

[27] S. Maintz, V. L. Deringer, A. L. Tchougréeff, and R. Dronskowski, LOBSTER: A tool to extract chemical bonding from plane-wave based DFT, J. Comput. Chem. **37**, 1030 (2016).

[28] S. L. Dudarev, G. A. Botton, S. Y. Savrasov, C. J. Humphreys, and A. P. Sutton, Electron-energy-loss spectra and the structural stability of nickel oxide: An LSDA+U study, Phys. Rev. B **57**, 1505 (1998).

[29] B. R. Ortiz, P. Gorai, L. Krishna, M. Rachel, A. Lopez, R. McKinney, V. Stevanović, and E. S. Toberer, Potential for high thermoelectric performance in n-type Zintl compounds: A case study of Ba doped $KAlSb_4$, J. Mater. Chem. A **5**, 4036 (2017).

[30] B. R. Ortiz, P. Gorai, V. Stevanovic, and E. S. Toberer, Thermoelectric performance and defect chemistry in n-type Zintl $KGaSb_4$, Chem. Mater. **29**, 4523 (2017).

[31] See Supplemental Material at http://link.aps.org/supplemental/10.1103/PhysRevMaterials.3.094407 for additional structural data, transport data, and calculations.

[32] B. R. Ortiz, K. Gordiz, L. C. Gomes, T. Braden, J. M. Adamczyk, J. Qu, E. Ertekin, and E. S. Toberer, Carrier density control in $Cu_2HgGeTe_4$ and discovery of Hg_2GeTe_4 via phase boundary mapping, J. Mater. Chem. A **7**, 621 (2018).

[33] C. M. Crawford, B. R. Ortiz, P. Gorai, V. Stevonovic, and E. S. Toberer, Experimental and computational phase boundary mapping of $Co_4Sn_6Te_6$, J. Mater. Chem. A **6**, 24175 (2018).

[34] S. Ohno, U. Aydemir, M. Amsler, J. H. Pöhls, S. Chanakian, A. Zevalkink, M. A. White, S. K. Bux, C. Wolverton, and G. J. Snyder, Achieving $zT > 1$ in inexpensive Zintl phase $Ca_9Zn_{4+x}Sb_9$ by phase boundary mapping, Adv. Funct. Mater. **27**, 1606361 (2017).

[35] S. Ohno, K. Imasato, S. Anand, H. Tamaki, S. D. Kang, P. Gorai, H. K. Sato, E. S. Toberer, T. Kanno, and G. J. Snyder, Phase boundary mapping to obtain n-type Mg_3Sb_2-based thermoelectrics, Joule **2**, 141 (2018).

[36] J. R. Neilson and T. M. McQueen, Bonding, ion mobility, and rate-limiting steps in deintercalation reactions with $ThCr_2Si_2$-type KNi_2Se_2, J. Am. Chem. Soc. **134**, 7750 (2012).

[37] T. M. McQueen, P. W. Stephens, Q. Huang, T. Klimczuk, F. Ronning, and R. J. Cava, Successive Orbital Ordering Transitions in $NaVO_2$, Phys. Rev. Lett. **101**, 166402 (2008).

[38] S. Lutfalla, V. Shapovalov, and A. T. Bell, Calibration of the DFT/GGA+ U method for determination of reduction energies for transition and rare earth metal oxides of Ti, V, Mo, and Ce, J. Chem. Theor. Comput. **7**, 2218 (2011).

[39] C. Weber, D. D. O'Regan, N. D. M. Hine, M. C. Payne, G. Kotliar, and P. B. Littlewood, Vanadium Dioxide: A Peierls-Mott Insulator Stable Against Disorder, Phys. Rev. Lett. **108**, 256402 (2012).

[40] C. E. Calderon *et al.*, The AFLOW standard for high-throughput materials science calculations, Comput. Mater. Sci. **108**, 233 (2015).

[41] K. Kadowaki and S. B. Woods, Universal relationship of the resistivity and specific heat in heavy-fermion compounds, Solid State Commun. **58**, 507 (1986).

[42] A. Jacko, J. Fjærestad, and B. Powell, A unified explanation of the Kadowaki-Woods ratio in strongly correlated metals, Nat. Phys. **5**, 422 (2009).